

Measurement of the temperature dependence of pulse lengths in an n-type germanium detector

I. Abt ^{a,*}, A. Caldwell ^a, J. Liu ^{a,b}, B. Majorovits ^a, O. Volynets ^a

^a*Max-Planck-Institut für Physik, München, Germany*

^b*now: Institute for the Physics and Mathematics of the Universe, Tokyo University, Tokyo, Japan*

Abstract

The temperature dependence of the pulse length was measured for an 18-fold segmented n-type germanium detector in the temperature range of 77 – 120 K. The interactions of 122 keV photons originating from a ¹⁵²Eu source were selected and pulses as observed on the core and segment electrodes were studied. In both cases, the temperature dependence can be well described by a Boltzmann-like *ansatz*.

Key words: germanium detectors, mobility, pulse shape, temperature dependence
PACS: 29.40.Gx Position-sensitive devices, 29.40.Wk Solid-state detectors

1 Introduction

High purity germanium detectors, HPGeDs, are widely used in spectroscopy, for example in the detection of low levels of radioactivity. They are also used in a wide variety of applications in particle and nuclear physics [1,2]. In particular, they are used for gamma ray tracking in arrays like AGATA [3] and GRETA [3], and in the search for neutrinoless double beta decay in experiments like GERDA [4] and MAJORANA [5].

For some applications, the shapes of the electric pulses collected on the electrodes are of interest. They are used in so called pulse shape analyses which

* Max-Planck-Institut für Physik, Föhringer Ring 6, 80805 München, Germany, Tel.: +49-(0)89-32354-295, FAX: +49-(0)89-32354-528

Email address: isa@mppmu.mpg.de (I. Abt).

are usually used to obtain information about event topologies. This can either help in gamma ray tracking [6] or in identifying background events [7,8].

A fundamental parameter of a pulse is its length. It can be used to measure the distance of the energy deposit from the electrodes. Its absolute value, however, depends also on the impurity density of the crystal and the relative location of the energy deposit with respect to the crystal axes. Other important factors are the mobilities, μ , of the charge carriers, electrons and holes, which are temperature, T , dependent.

The mobilities of the charge carriers have been measured in the past. However, the results, obtained for different samples, do not completely agree [9]. In principle, the mobilities can be determined by comparing measured to simulated pulses. In practice, this is difficult, because the impurity density distribution of a detector crystal is also not precisely known.

The T dependence of the mobilities, can be directly related to the T dependence of the pulse lengths. Photon interactions from the 122 keV line of a ^{152}Eu source were used to select charge depositions close to the outer surface of an n-type cylindrical true-coaxial germanium detector. Holes created close to the surface quickly drift to the mantle electrode and the electrons drifting to the core determine the total length of the pulse. The holes influence only the first part of the pulse. Pulses were studied separately for interactions close to the crystallographic axes $\langle 110 \rangle$ and $\langle 100 \rangle$.

2 Experimental Setup

The detector used was a cylindrical true-coaxial 18-fold (6ϕ , $3z$) segmented n-type detector with a height of 70 mm and a diameter of 75 mm. It was manufactured by Canberra France and is similar to the detector previously characterized in detail [10]. The inner bore had a diameter of 10 mm. The density of electrically active impurities was given by the manufacturer as $0.35 \cdot 10^{10}/\text{cm}^3$ at the top and $0.55 \cdot 10^{10}/\text{cm}^3$ at the bottom of the detector. The change in impurities is assumed to be linear with height, z . The operational voltage was 2000 V.

The detector was mounted either inside a vacuum cryostat [10], K1, or submerged in a liquid nitrogen volume [11], GII. In both cases, a collimated 40 kBq ^{152}Eu source with a 1σ beam spot diameter of about 5 mm was used. The coordinate system used was cylindrical with the origin at the geometric center of the detector and $\phi = 0$ along its crystallographic $\langle 110 \rangle$ axis.

The detector T inside GII was constantly 77.4 K while it was increasing with

time inside K1, where it was cooled via a cooling finger submerged in a liquid nitrogen reservoir. When the reservoir was not refilled, the detector slowly warmed up. The temperature, T_{mon} , was monitored with a thermal resistor, PT100, mounted as close as possible to the detector inside K1. The temperature, T , of the detector was expected to be higher by $\Delta T = T - T_{\text{mon}}$ between 4 – 10 K.

The following datasets were analysed:

- DS1: detector operated in GII, submerged in LN2, $T = 77.4$ K;
- DS2: detector operated in K1, vacuum, $95 \text{ K} < T_{\text{mon}} < 100 \text{ K}$;
- DS3: detector operated in K1, vacuum, $100 \text{ K} < T_{\text{mon}} < 120 \text{ K}$.

The measurements in K1 were started after the initial cool-down of the setup. They were performed while the detector was warming up. For DS2, T_{mon} was monitored during breaks in the data taking. The value of T_{mon} is interpolated for intermediate times. For DS3, the time dependence of T_{mon} was taken from test warm-ups where T_{mon} was measured in one minute intervals. Figure 1 shows the temperature development for one measurement of DS2 and two test warm-ups for DS3, one at the beginning and one at the end of the DS3 data taking.

The absolute value of T_{mon} for DS3 depended on the initial T_{mon} . The development of T_{mon} with time was however stable. The T_{mon} could thus be extrapolated from the initial T_{mon} for each measurement cycle.

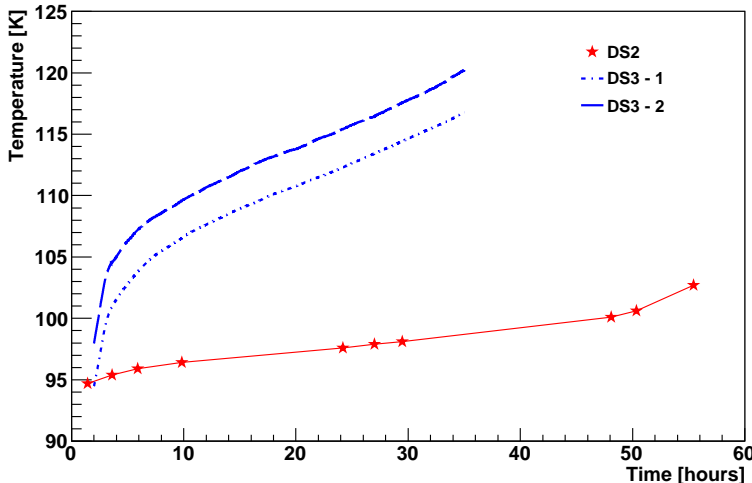


Fig. 1. Development of T_{mon} for one of the measurements of DS2 and two test warm-ups for DS3.

Data were grouped into 15-minute intervals. For the analysis, it was assumed that T and T_{mon} were constant during these intervals. At the beginning of the measurements in DS3 the steep rise in T_{mon} was excluded.

Measurements were taken separately around the $\langle 110 \rangle$ axis at $\phi = 0^\circ$ and the $\langle 100 \rangle$ axis at $\phi = 45^\circ$. The measurements for DS3 were 5° off axis. The restrictions of the GII setup did not allow a measurement on the $\langle 100 \rangle$ axis. Additional data were taken for cross-checks. Table 1 provides an overview. The two axes were located in different segments of the detector. None of the axes was close to a segment boundary. A schematic of the setup is shown in Fig. 2.

	orientation	DS1	DS2	DS3
A1	$\langle 110 \rangle$	0°	0°	5°
A2	$\langle 100 \rangle$		45°	50°
C1	$\langle 110 \rangle +5^\circ$	5°		5°
C2	$\langle 110 \rangle -15^\circ$	-15°		-15°

Table 1
Datasets A1 and A2, entering the analysis, and C1 and C2, used for cross checks

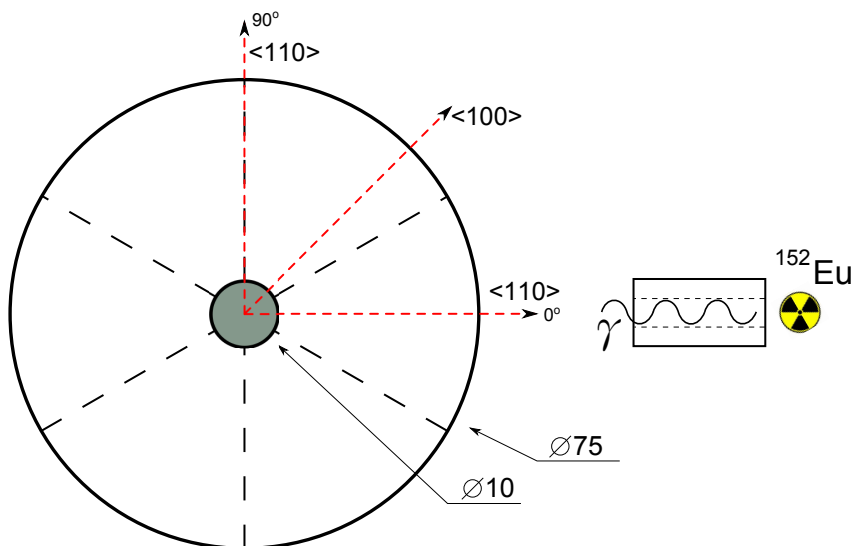


Fig. 2. Schematic of the measurement setup. Long- and short-dashed lines indicate the segment boundaries and crystallographic axes.

The core and all 18 segments, 19 channels, were connected to charge sensitive preamplifiers, PSC 823, produced by Canberra-France. The preamplifiers and the cables limit the bandwidth of the system to about 10 MHz. The energies and pulse forms were recorded for all 19 channels using a “DGF Pixie-4” data acquisition system, DAQ, manufactured by X-Ray Instrumentation Associates, XIA. The core pulse was always used to trigger. The DAQ has 14-bit ADCs and a sampling frequency of 75 MHz [12].

3 Pulse shape simulation

Two simulated pulses, one for the core and one for the segments, were used as references to determine the relative lengths and amplitudes of measured pulses. They were generated using the pulse shape simulation package [13] developed for true-coaxial detectors.

The pulses were simulated for a point-like energy deposit of 122 keV at $r = 32.5$ mm, $\phi = 0^\circ$ and $z = 0$ mm. This point is located on the $\langle 110 \rangle$ axis of the detector, 5 mm deep inside the detector. The depth was chosen as it is the average penetration depth of 122 keV photons.

The parameters of the simulation were:

- impurity level of $0.45 \cdot 10^{10} / \text{cm}^3$, corresponding to the specification at $z = 0$ mm;
- electron mobility [9], corresponding to $T = 77$ K;
- grid for numerical field calculations of $32(r) \times 180(\phi) \times 70(z)$;
- time, t , development in steps of 1 ns, corresponding to spatial steps of about $100 \mu\text{m}$ which is the granularity needed to reflect the development of charge trajectories;
- bandwidth of 10 MHz and amplifier decay time of $50 \mu\text{s}$;
- no noise.

The simulated charge pulses, $C_{\text{sim}}^{c,s}$, for core, c , and segments, s , are shown in Fig. 3. The amplitude is normalized to ± 1 , respectively. The pulses start at $t=100$ ns and have a total rise time, t_r , of almost 400 ns. The times, at which the pulses reach 10% and 90% of their amplitudes, are indicated. The time interval inbetween, the so called 10–90 rise-times, $t_r^{c,s:10-90}$, differ for core and segments. The $t_r^{c,s:10-90}$ were used in all measurements to evaluate the length of a pulse, because the beginning and the end of a pulse are very susceptible to noise.

The usage of a reference pulse, simulated as one interaction 5 mm inside the detector, instead of an average over pulses simulated according to beamspot and penetration depth, does not change $t_r^{c:10-90}$ significantly [13]. The effect on $t_r^{s:10-90}$ will be subject of a separate investigation. In general, the hole drift is less well understood than the electron drift. This is reflected in a less accurate prediction of the detailed pulse shape for the segments.

The simulated core and segment pulses along $\langle 110 \rangle$ at 77.4 K have $t_r^{c:10-90} = 290$ ns and $t_r^{s:10-90} = 239$ ns.

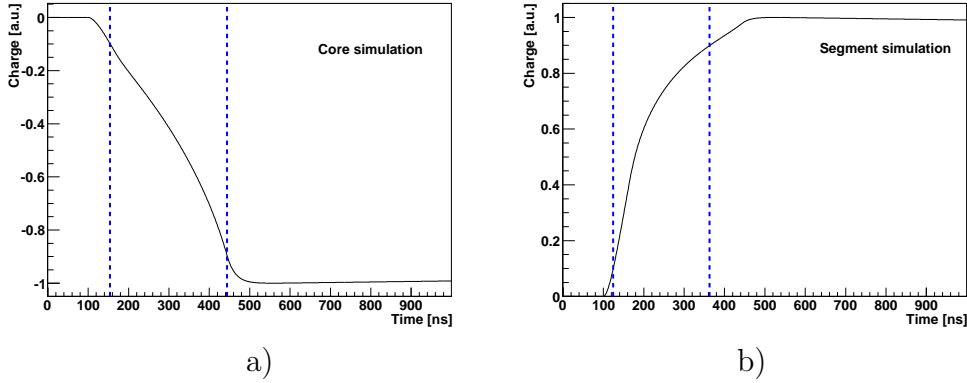


Fig. 3. Simulated reference pulses for a) core and b) segments. The pulses are normalized to ± 1 . The times at which 10% and 90% of the amplitude are reached are indicated by dashed lines.

4 Model expectations

The T dependence of the rise time is assumed to be due to the T dependence of the mobility of the charge carriers. The velocity, $\vec{v}_{e/h}(\vec{x})$ of the charge carrying electrons, e , and holes, h , at each point $\vec{x} = (r, \phi, z)$ is given by

$$\vec{v}_{e/h}(\vec{x}) = \frac{\mu_{e/h} \vec{E}(\vec{x})}{[1 + (\frac{|\vec{E}(\vec{x})|}{E_0})^\beta]^{1/\beta}} \quad , \quad (1)$$

where $\mu_{e/h}$ is the charge carrier mobility tensor, $\vec{E}(\vec{x})$ is the electric field and E_0 and β are fit parameters obtained in measurements [9] along the crystallographic axes. The mobility tensor depends on the relative position of \vec{x} to the crystallographic axes. Along the axes, $\mu_{e/h}$ becomes a number. A more detailed discussion relevant for the detector considered here can be found elsewhere [13].

As the detector is true-coaxial, \vec{E} is radial with the absolute value, $E(r)$. Thus, the velocity, $v_{e/h}(r)$, becomes radial along the crystallographic axes. Due to the extremely low impurity density, $E(r)$ varies by less than 50% over r [13, Fig.1]. Thus it is appropriate to use the approximation

$$v_{e/h}(r) = \mu_{e/h}^{\text{eff}} E(r) \quad , \quad (2)$$

where $\mu_{e/h}^{\text{eff}}$ are the effective mobilities of the charge carriers.

The differential equations, $v_{e,h}(t) = dr_{e,h}(t)/dt$, for the radial drift, $r_{e,h}(t)$, of the electrons and holes along a crystallographic axis can be solved. In the case

considered here, the electron drift dominates and any T dependence, $\mu_e^{\text{eff}}(T)$, is directly reflected in a T dependence of the rise time, $t_r(T)$, which becomes

$$t_r(T) = \frac{C_{\text{det}}}{\mu_e^{\text{eff}}(T)}, \quad (3)$$

where C_{det} is a constant that was calculated from the detector geometry and its electrical parameters after solving the equations. For the detector under consideration it is $C_{\text{det}} = 5.9 \cdot 10^{-3} \text{ cm}^2/\text{V}$.

It is generally assumed that $\mu_e^{\text{eff}}(T)$ can be described as

$$\mu_e^{\text{eff}}(T) = \mu_e^T f(T), \quad (4)$$

where μ_e^T is a constant, f is some functional form and T is given in Kelvin. Models based on the scattering of electrons and holes off the phonons in the lattice [14] suggest a form of $f(T) = T^{-3/2}$. This is qualitatively supported by some measurements at higher impurity levels [15, p. 108]. Other measurements, also at higher impurity levels, show a behavior of $f(T) = T^{-1.6}$ or $f(T) = T^{-1.66}$ [16].

The values of the electron mobility used in the simulation for the $\langle 110 \rangle$ axis at 77 K can be translated into a value for $\mu_e^{\text{eff}}(77 \text{ K})$ of $1.4 \cdot 10^4 \text{ cm}^2/(\text{Vs})$. For $f(T) = (T/\text{K})^{-3/2}$, the constant μ_e^T becomes $\mu_e^T = 9.4 \cdot 10^6 \text{ cm}^2 /(\text{Vs})$. This provides an absolute model prediction to be compared to data. As it is not expected that the shapes of the pulses for core and segment vary significantly within the T range, it also provides a prediction for $t_r^{c,s:10-90}$.

5 Event selection

Events induced by 122 keV photons were selected using the energies measured in the individual segments. Single segment events were selected by requiring energy deposits of less than 20 keV in all other segments. Figure 4 shows the spectrum around 122 keV of the segment containing the $\langle 110 \rangle$ axis for single segment events from DS3 at $T_{\text{mon}}=104 \text{ K}$. The width of the peak was determined by a fit of a Gauss function and events within $\pm 2\sigma$ were selected. Typical signal to background ratios were 3:1 to 5:1 for DS2 and DS3 and 1:1 to 2:1 for DS1.

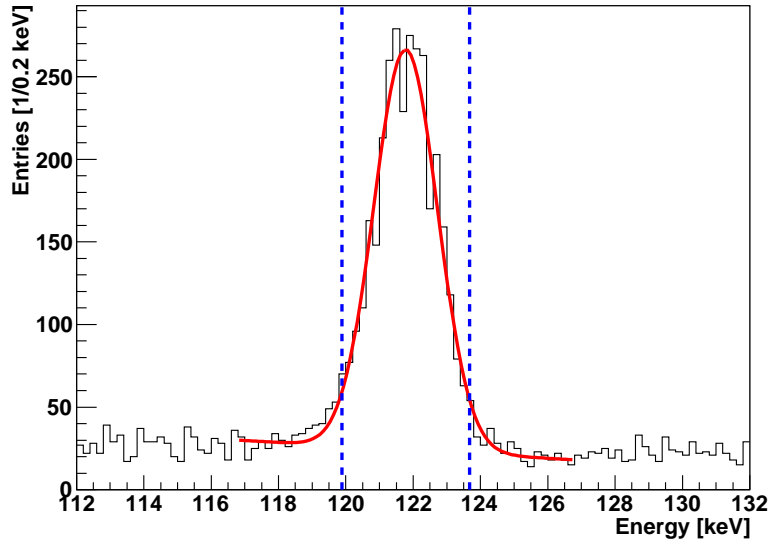


Fig. 4. Energy spectrum around the 122 keV peak as measured by the segment on the $\langle 110 \rangle$ axis. Also shown is a fit with a Gauss function plus a first-order polynomial. The 2σ limits are shown as dashed lines.

6 Rise time determination

The rise time of a measured pulse was not extracted directly because of the noise level observed during the measurements. Instead, a fitting procedure was used, where a simulated pulse was fitted to the measured pulse as a reference. This method was chosen, because it uses the full information of the measurement and is robust against noise which averages out.

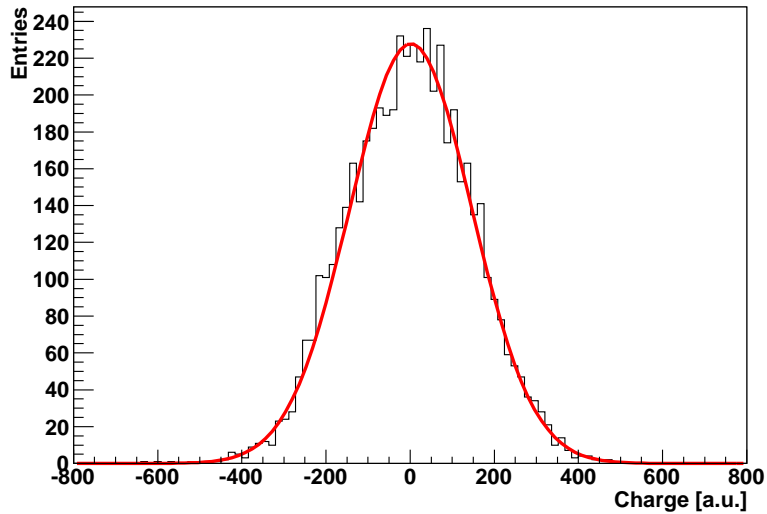


Fig. 5. Typical noise distribution in arbitrary units. Also shown is a Gaussian fit.

Before the fit, the baseline was subtracted from each pulse. It was calculated as the average of the values recorded for the first 15 bins, 200 ns, of the pulse record. This was possible, because the DAQ was adjusted to record pulse information starting 200 ns before the trigger time.

The noise level for each 15-minute interval was determined using the first 200 ns of several hundred baseline subtracted pulses. Figure 5 shows a typical noise distribution. The unit of the charge is arbitrary. The noise is clearly Gaussian. Its level was typically about 3% of the pulse amplitude. Each point of a measured pulse was assigned an uncertainty corresponding to the noise level of the dataset.

The simulated pulses, $C_{\text{sim}}^{c,s}$, were fitted separately to the measured core and segment pulses:

$$C_{\text{meas}}^{c,s}(t) = A^{c,s} \cdot C_{\text{sim}}^{c,s}(t/t_{\text{scale}}^{c,s} + t_{\text{offset}}^{c,s}), \quad (5)$$

where the fitted parameters are the relative amplitudes, $A^{c,s}$, the time offsets of the measured pulses, $t_{\text{offset}}^{c,s}$, and the time scaling factors $t_{\text{scale}}^{c,s}$. The important parameters are $t_{\text{scale}}^{c,s}$ which were converted into measured values of $t_r^{c,s:10-90}$.

Only good fits were considered. A fit was qualified as good, if $\chi^2/\text{ndf} \leq \chi_{c,s}^2$. The values for $\chi_{c,s}^2$ were chosen to reject 50% of the pulses corresponding to the worst background levels observed. They were adjusted for each dataset and where 1.1(2.0) for DS1, 1.2(1.7) for DS2 and 1.7(1.9) for DS3 for the core (segment). Figures 6 and 7 show examples of two events with good and bad fits for both core and segment pulses.

A bad fit could indicate that the interaction point was not close to the outer mantle. This can happen when a 122 keV photon penetrates deeper than in average or, if the event results from an interaction associated to the Compton background. The background also contains multiple interactions.

The distributions of the fit parameters $t_{\text{scale}}^{c,s}$ for all good fits were fitted with Gauss functions and the resulting means, $t_{\text{scale-mean}}^{c,s}$, are converted to measured $t_r^{c,s:10-90}$ values for a given position and temperature.

Figure 8 shows the t_{scale}^c distribution for the core pulses along the $\langle 110 \rangle$ axis at 77.4 K. The resulting $t_{\text{scale-mean}}^c$ is very close to 1 and results in a measured pulse length of $t_r^{c:10-90} = 287 \pm 2$ ns. The uncertainty is statistical only.

The measured value for the segment is $t_r^{s:10-90} = 305 \pm 2$ ns. The agreement between simulation and measurement is excellent for the core while it is quite poor for the segments. The discrepancy might be explained by a combination of the poor understanding of the hole mobility and net charge carrier density

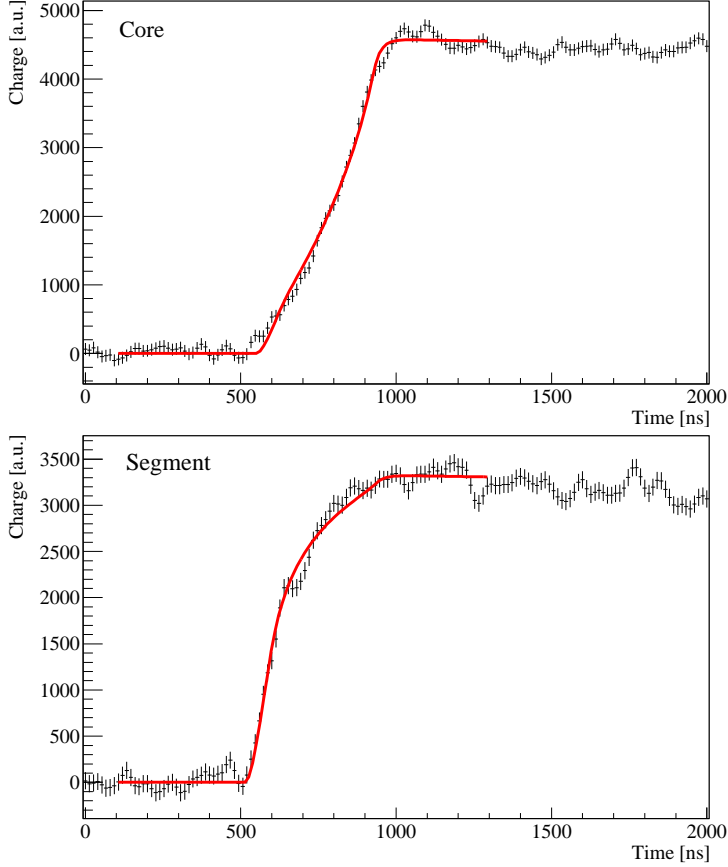


Fig. 6. Pulses in core and segment of a typical event from DS3 at $T_{\text{mon}} = 100$ K. The fits with the simulated pulses are also shown. The fits are classified as good with $\chi^2/\text{ndf} = 1.06(1.05)$ for the core(segment).

variations close to the core. The hole mobility determines the time when the 10 % level is reached. The 90 % level could be influenced by a changing drift velocity of the electrons close to the core due to changing impurity levels. The segment pulses would be affected more than the core pulses due to the different strengths of weighting fields. The relative discrepancy should, however, not change within the temperature range considered.

7 T dependence

The values of $t_r^{c,s:10-90}$ as determined according to the procedure described in the previous section were used to study the temperature dependence of the rise time. The analysis was performed separately for the two crystallographic axes $\langle 110 \rangle$ and $\langle 100 \rangle$ using the datasets A1 and A2 from Table 1. The drift along $\langle 100 \rangle$ is known to be faster at 77 K [9]. The T dependence is *a priori* assumed to be the same.

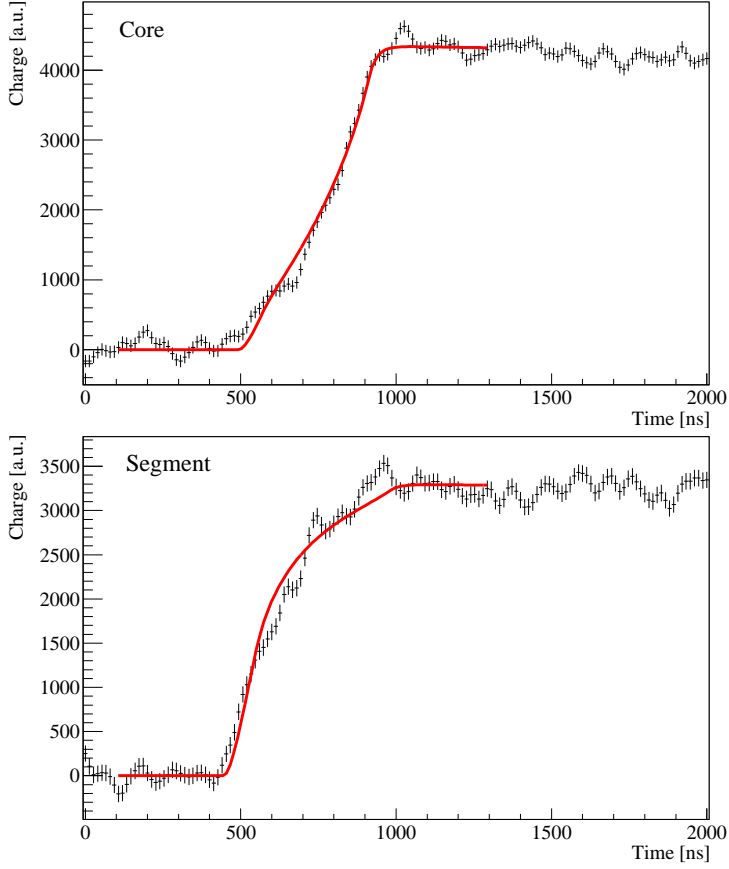


Fig. 7. Pulses in core and segment of a typical event from DS3 at $T_{\text{mon}} = 100$ K. The fits with the simulated pulses are also shown. The fits are classified as bad with $\chi^2/\text{ndf} = 1.87(2.29)$ for the core(segment).

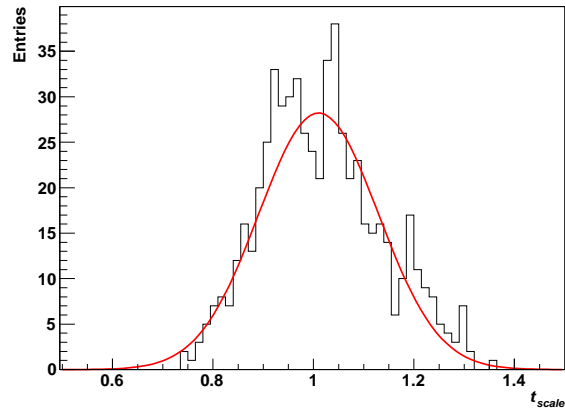


Fig. 8. Distribution of the scaling parameter t_{scale}^c for measured core pulses along the $\langle 110 \rangle$ at 77.4 K. Also shown is a Gaussian fit.

As explained in section 2, T is only known up to a measurement dependent shift ΔT for DS2 and DS3. When a functional form f , as introduced in Equation 4, was fitted to rise-time data including DS2 or DS3, free parameters $\Delta T^{2,3}$ were introduced to the fit, respectively.

Figure 9 shows the development of $t_r^{c:10-90}$ for the $\langle 110 \rangle$ axis together with the model prediction from section 4,

$$t_r(T) = \frac{C_{\text{det}}}{\mu_e^T} T^{3/2} \quad , \quad (6)$$

and a fit with a simple Boltzmann-like *ansatz*

$$t_r(T) = p_0 + p_1 e^{-p_2/T} \quad , \quad (7)$$

where p_0 , p_1 , p_2 are free parameters.

The model prediction does not describe the data at all. It correctly predicts the value of $t_r^{c:10-90}$ at 77.4 K, but it is clear that the predicted T dependence is not observed in the data. The description cannot be improved by modifying the exponent. The more general *ansatz* $t_r(T) = p_0 + p_1 T^{p_2}$ can also not describe the data. The description is bad in the T range of DS2 and DS3 and completely misses the DS1 point. However, the Boltzmann-like *ansatz* describes the data quite well. This is also true for the segment pulses as shown in Fig. 10. For the segment pulses, the model prediction from section 4 neither describes the T dependence nor the point at 77 K. The hole drift is more important in this case and as mentioned in section 3 the parameters for the hole drift are less well measured.

The situation for the $\langle 100 \rangle$ axis is shown in Figs. 11 and 12. No data were available at 77 K. However, it is clear that a power law cannot describe the data for either core or segment, while a Boltzmann-like *ansatz* can be fitted quite well.

The success of the Boltzmann-like *ansatz* could be connected to a change in the conductivity of the germanium crystal [17] in the T range considered. This might have affected the electric field strongly, because the detector was operated relatively closely to the full depletion voltage.

Table 2 lists the values obtained in χ^2 -fits for the parameters p_1 and p_2 from Equation 7 which are strongly correlated. The values for p_2 are also shown as energies, E , with $p_2 = E/(2k)$, where k is the Boltzmann constant. The uncertainties given are statistical only. The χ^2/ndf is typically around 5.

The core and segment parameters agree within statistical uncertainties for

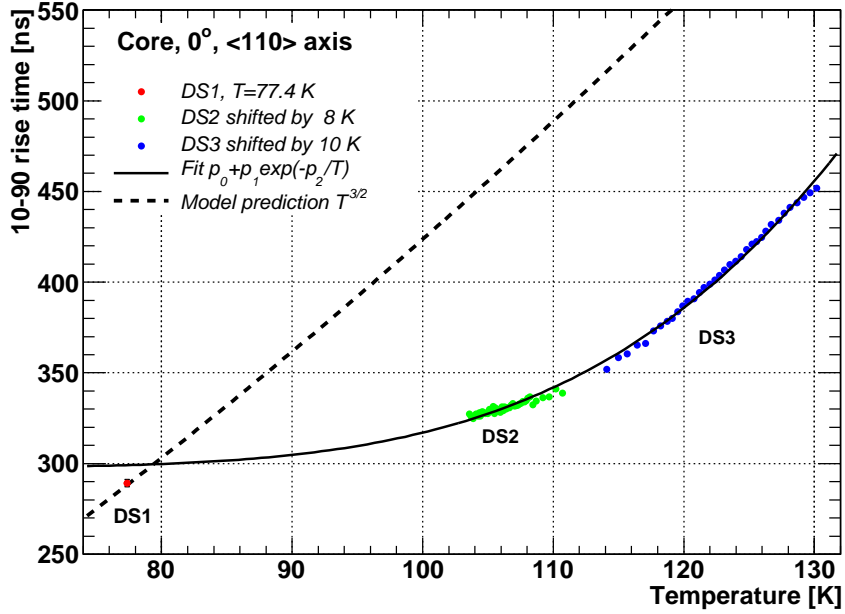


Fig. 9. Dependence of $t_r^{c:10-90}$ on T along the $\langle 110 \rangle$ axis. Also shown are the model prediction described in section 4 and a fit with a Boltzmann-like *ansatz*. Statistical uncertainties are smaller than the symbol size.

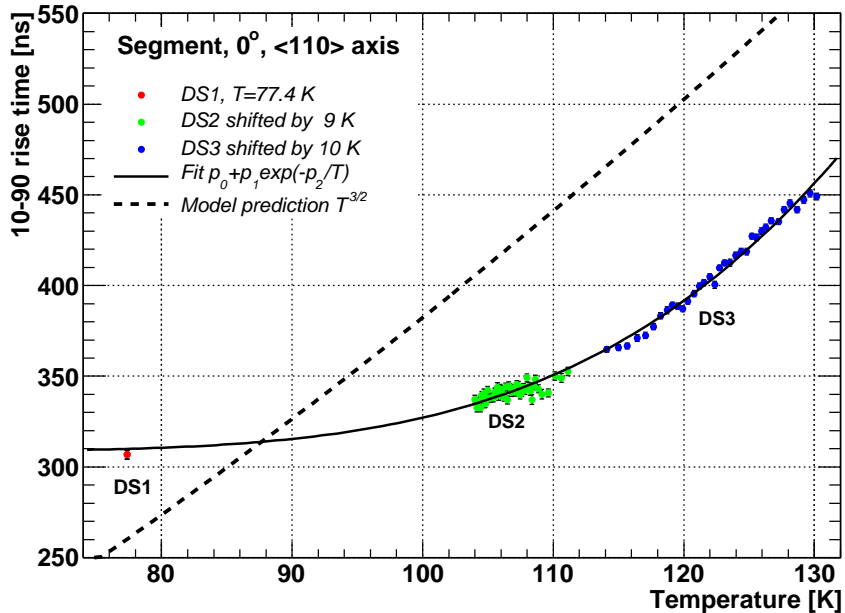


Fig. 10. Dependence of $t_r^{s:10-90}$ on T along the $\langle 110 \rangle$ axis. Also shown are the model prediction described in section 4 and a fit with a Boltzmann-like *ansatz*. Statistical uncertainties are shown, but are mostly smaller than the symbol size.

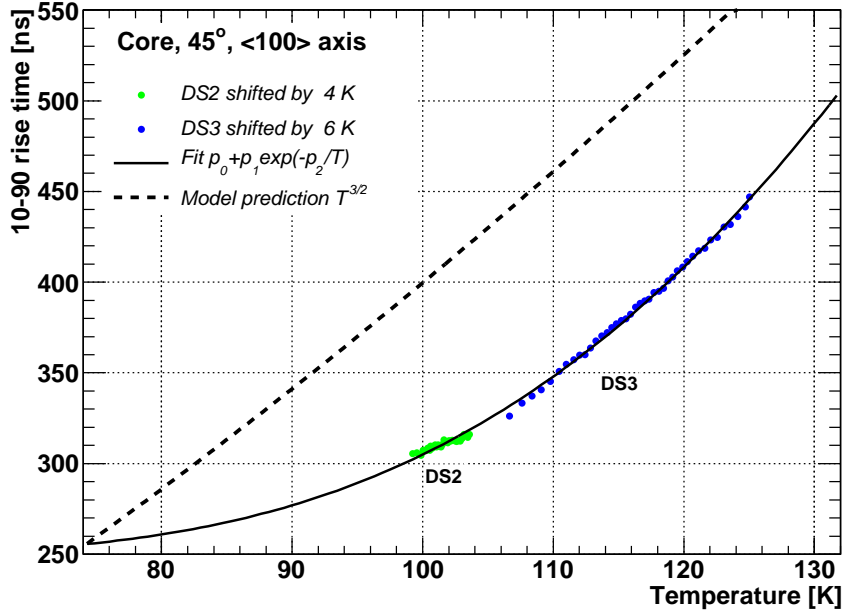


Fig. 11. Dependence of $t_r^{c:10-90}$ on T along the $\langle 100 \rangle$ axis. Also shown are the model prediction described in section 4 and a fit with a Boltzmann-like *ansatz*. Statistical uncertainties are smaller than the symbol size.

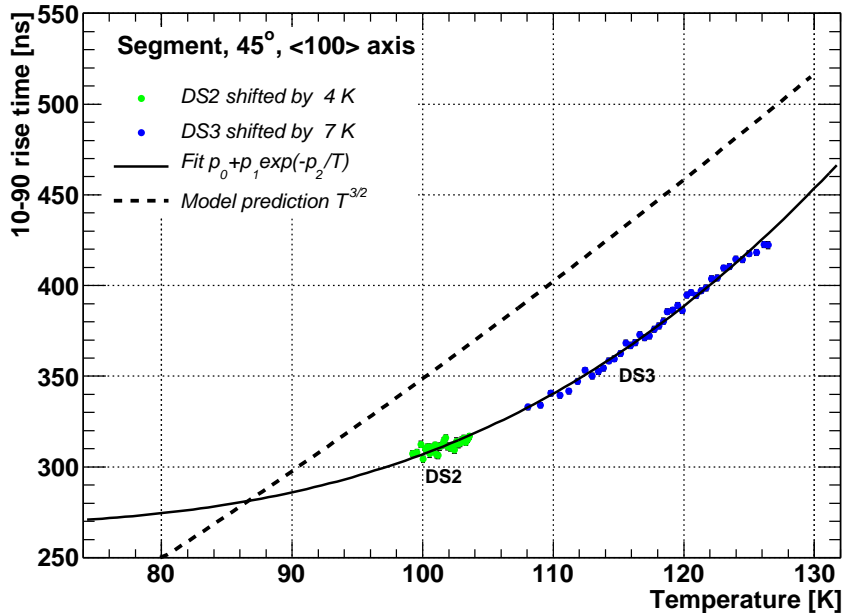


Fig. 12. Dependence of $t_r^{s:10-90}$ on T along the $\langle 100 \rangle$ axis. Also shown are the model prediction described in section 4 and a fit with a Boltzmann-like *ansatz*. Statistical uncertainties are shown, but are mostly smaller than the symbol size.

Table 2

Fit parameters determined for a Boltzmann-like *ansatz* using the datasets A1, A2, C1 and C2

	orientation	c, s	p_1 [$\cdot 10^4$]	p_2	E [meV]
A1	$\langle 110 \rangle$	c	17.7 ± 1.3	913 ± 10	158 ± 2
A1	$\langle 110 \rangle$	s	15.0 ± 2.3	900 ± 20	155 ± 4
A2	$\langle 100 \rangle$	c	3.0 ± 0.2	630 ± 8	109 ± 2
A2	$\langle 100 \rangle$	s	3.1 ± 0.4	666 ± 18	115 ± 3
C1	$\langle 110 \rangle + 5^\circ$	c	3.5 ± 0.3	649 ± 12	112 ± 2
C1	$\langle 110 \rangle + 5^\circ$	s	5.6 ± 0.7	725 ± 18	125 ± 3
C2	$\langle 110 \rangle - 15^\circ$	c	5.5 ± 0.5	705 ± 13	122 ± 2
C2	$\langle 110 \rangle - 15^\circ$	s	5.5 ± 0.9	732 ± 22	126 ± 4

the datasets A1 and A2, respectively. However, the parameters for the two axes seem to be significantly different. A cross-check for the $\langle 110 \rangle$ axis, using dataset C1 from Table 1, did, however, not confirm this. The parameters should be the same, but they agree better with the parameters of the fit to A2. The inclusion of DS2 is what pushes the values of p_1 and p_2 up in the fit to A1. As the absolute temperatures for DS2 and DS3 are not known, but have to be fitted, we used this cross-check to estimate the systematic uncertainty on E to be ≈ 40 meV. The systematic uncertainty could also be connected to the misalignment present for DS3, even though such a strong deviation is not expected for a 5° offset. Another cross-check was performed using the dataset C2. At that position, the drift is not simply radial any more due to the distance from the crystallographic axes [13, Fig.3], but the data could still be described by the Boltzmann-like *ansatz*. The fit results for C2 and C1 are compatible.

The fits were further analysed using the program package BAT [18]. The values listed in Table 2 were confirmed by BAT as the global mode. A detailed study of the probability densities revealed that the inclusion of DS2 causes elongated two-dimensional probability densities with local minima, also pointing to systematic uncertainties of up to ≈ 40 meV for the fits to A1 and A2. The probability densities for the fits to C1 and C2 are much more regular, pointing at systematic uncertainties of less than ≈ 20 meV.

The drift along the two crystallographic axes were expected to have the same T dependence. The data, independent of fitting procedures, seem to indicate that the T dependence of the “slow axis”, $\langle 110 \rangle$, is less pronounced. At some T , the rise time along the “fast axis”, $\langle 100 \rangle$, seems to become as large as along the “slow axis”. A definite conclusion would need better data. More

measurements at more angles and with an improved temperature monitoring are planned.

It should be noted that while the rise times changed with temperature, the amplitudes remained stable, even to the highest temperature of about 130 K. This means that the detector could be operated stably at temperatures well above 100 K.

8 Summary

The temperature dependence of the rise time of pulses was studied between 77 K and 130 K. The data cannot be described by the expected $T^{-3/2}$ dependence of the charge carrier mobilities. Both core and segment pulses display a Boltzmann-like temperature dependence of the rise time.

The significant temperature dependence of the rise time should be taken into account when pulses are simulated for specific experimental setups or used in pulse shape analyses. It should be noted that the detector used for the investigation could be stably operated up to temperatures of 130 K without an observable change in the energy scale.

References

- [1] G. F. Knoll, *Radiation Detection and Measurement* third ed., (Wiley, New York 1999) 423
- [2] J. Eberth and J. Simpson, *Prog. Part. Nucl. Phys.* **60** (2008) 283
- [3] I-Yang. Lee and J. Simpson, *Nucl. Phys. News* , **20**, Issue 4, 23
- [4] I. Abt *et al.*, arXiv:hep-ex/0404039v1 and S. Schönert *et al.*, [GERDA Collab.], *Nucl. Phys. Proc. Suppl.* **145** (2005) 242
- [5] C.E. Aalseth *et al.*, [MAJORANA Collaboration], *Nucl. Phys. B (Proc. Suppl.)* **138** (2005) 217
- [6] O. Wieland *et al.*, *IEEE Trans. Nucl. Sc.* **48** (2001) 296
- [7] S. R. Elliott *et al.*, *Nucl. Instr. Meth. A* **558** (2006) 504
- [8] I. Abt *et al.*, *Eur. Phys. J. C* **52** (2007) 19
- [9] B. Bruyneel *et al.*, *Nucl. Instr. Meth. A* **569** (2006) 764
- [10] I. Abt *et al.*, *Nucl. Instr. Meth. A* **577** (2007) 574

- [11] I.Abt *et al.*, J. Instr **4** (2009) 11008
- [12] http://www.xia.com/DGF_Pixie-4_Download.html
- [13] I. Abt *et al.*, Eur. Phys. J. C **68** (2010) 3
- [14] J. Bardeen and W. Shockley, Phys.Rev. **80** (1950) 72
- [15] M.S.Tyagi, *Introduction to semiconductors materials and devices*, John Wiley&Sons, (1991)
- [16] M.B. Prince, Phys.Rev. **92** (1954) 681
F.J. Morin, Phys.Rev. **93** (1954) 62
- [17] K. Irmscher, private communication, Leibniz-Institut fuer Kristallzüchtung, Berlin
- [18] A. Caldwell, D. Kollar, K. Kröniger, Comp. Phys. Com. **180** (2009) 2197